Quasi-3D Cytoskeletal Dynamics of Osteocytes under Fluid Flow

Andrew D. Baik,[†] X. Lucas Lu,[†] Jun Qiu,[†§] Bo Huo,[¶] Elizabeth M. C. Hillman,[‡] Cheng Dong,[∥] and X. Edward Guo[†*]
[†]Bone Bioengineering Laboratory and [‡]Laboratory for Functional Optical Imaging, Department of Biomedical Engineering, Columbia University, New York, New York; [§]School of Aerospace, Tsinghua University, Beijing, People's Republic of China; [¶]Institute of Mechanics, Chinese Academy of Sciences, Beijing, People's Republic of China; and [∥]Department of Bioengineering, Pennsylvania State University, University Park, Pennsylvania

ABSTRACT   Osteocytes respond to dynamic fluid shear loading by activating various biochemical pathways, mediating a dynamic process of bone formation and resorption. Whole-cell deformation and regional deformation of the cytoskeleton may be able to directly regulate this process. Attempts to image cellular deformation by conventional microscopy techniques have been hindered by low temporal or spatial resolution. In this study, we developed a quasi-three-dimensional microscopy technique that enabled us to simultaneously visualize an osteocyte's traditional bottom-view profile and a side-view profile at high temporal resolution. Quantitative analysis of the plasma membrane and either the intracellular actin or microtubule (MT) cytoskeletal networks provided characterization of their deformations over time. Although no volumetric dilatation of the whole cell was observed under flow, both the actin and MT networks experienced primarily tensile strains in all measured strain components. Regional heterogeneity in the strain field of normal strains was observed in the actin networks, especially in the leading edge to flow, but not in the MT networks. In contrast, side-view shear strains exhibited similar subcellular distribution patterns in both networks. Disruption of MT networks caused actin normal strains to decrease, whereas actin disruption had little effect on the MT network strains, highlighting the networks' mechanical interactions in osteocytes.

INTRODUCTION

Osteocytes are three-dimensional (3D), ellipsoidal, mature bone cells encased in mineralized extracellular matrix. Abundant evidence has shown that the osteocytes are the key mechanonsensors in bone that directly regulate bone-forming osteoblast and bone-removing osteoclast activities (1–3). It has been hypothesized that the dominant loading mechanism of the mechanosensing osteocytes is oscillating fluid shear stress resulting from the mineralized matrix deformation of bone (4). Most in vitro fluid shear studies on primary osteocytes and osteocyte cell lines have focused on monolayers of flat, spread osteocytes, but the in vivo shape of osteocytes is ellipsoidal or spherical (5). In vitro experiments have demonstrated that osteocytes are more mechanosensitive in this 3D configuration than when they are flat and spread (6). Recent experimental and theoretical evidence suggests a subcellular location-dependent responsiveness to fluid shear in the osteocyte (7,8). However, the 3D intracellular deformation and mechanics of an osteocyte under fluid flow is poorly characterized. Conventional bottom-view, two-dimensional (2D) microscopy of an ellipsoidal osteocyte cell is insufficient for characterizing the intracellular deformation of the adhered cells at their apical surface and their basal surface under flow (9).

Actin and microtubule (MT) cytoskeletons have been shown to play an important role in the osteocyte's biochemical response to fluid shear loading (10,11). Mechanical inter-

actions between the two networks have profound effects on the behavior of each individual network (12). Reconstituted cytoskeleton studies have investigated how mechanical coupling affects each network's mechanical properties (13), but studies in live cells are lacking. Recent evidence has established the importance of studying the mechanics of whole, aggregate cytoskeletal networks in the context of a living cell rather than just individual filaments (14). For example, network deformation of MTs has been shown to be a direct mediator in the spatial activation of Src in smooth muscle cells (15). Furthermore, this activation occurs on the millisecond timescale after mechanical stimulus, emphasizing the importance of the initial deformational events. Therefore, the network deformational dynamics of actin and MT cytoskeletons and their interactions under mechanical loading by fluid shear deserve further characterization and study.

Traditional techniques to obtain 3D images of a cell body, such as confocal or deconvolution microscopy, are inherently timescale-limited due to the necessity of scanning a z-stack. Obtaining sufficient 3D osteocyte information by laser scanning confocal microscopy takes ~0.5–0.8 s. This imaging frequency would drastically undersample the instantaneous deformational responses of bone cells, especially under physiological oscillatory flow profiles (16). A promising technique to obtain additional spatial information while maintaining a high temporal resolution is to view the cell from the side. Several studies have imaged cells in side-view for various applications, including cell adhesion/detachment (17–19) and atomic force microscopy (20). However, these studies were not capable of simultaneously

imaging the traditional inverted microscope-based bottom-view at high spatial or temporal resolution.

In this study, we used a quasi-3D imaging system to simultaneously image two orthogonal planes (the traditional bottom-view plane and a side-view plane) of a single osteocyte under fluid flow. With this approach, we were able to overcome the limitations of traditional bottom-view 2D microscopy and obtain far more spatial information than was previously possible. This quasi-3D system avoids the use of z-stack raster scanning for confocal microscopy, allowing the temporal resolution to be limited only by the camera frame rate. The objectives of this study were to 1), develop a quasi-3D microscopy system to allow simultaneous bottom- and side-view visualization of a single cell under fluid flow; 2), visualize osteocyte actin or MT networks along with the whole-cell shape under fluid shear; and 3), compare the network deformation of actin and MT networks and characterize their mechanical interactions.

MATERIALS AND METHODS

Microscope/quasi-3D imaging

A custom-designed dual-microscope system consisting of an IX-71 inverted microscope and a BX-2 upright microscope (Olympus America, Center Valley, PA) was utilized in this study. A custom-built holder was used to align a 45° mirror in the light path (17,21) of the upright microscope so that side-view images of a single cell could be obtained while the inverted microscope simultaneously obtained regular bottom-view images of the same cell (Fig. 1 A). The cell was imaged in a glass tube (Vitrocom, Mountain Lakes, NJ) with a square cross-section, which provided perpendicular glass planes for high-resolution imaging and also served as a fluid flow chamber. Both microscopes used 60X LUCPLNFLN long working distance objective lenses (Olympus America). A Lambda DG-4 xenon light source (Sutter, Novato, CA) attached to the inverted microscope was used to switch between two excitation filters (Semrock, Rochester, NY) to excite either green fluorescent protein (GFP; 475/35) or Alexa Fluor 594 (580/23). The xenon lamp output was attenuated by 50%, and an additional 50% neutral density filter was used to minimize phototoxicity of the cells.

Dual-bandpass emission filters for GFP and Alexa Fluor 594 emissions (527/42 and 645/49) and corresponding dichroics in each microscope filtered the appropriate light bands, and ORCA-AG interline CCD cameras (Hamamatsu, Japan) with 2×2 binning in each microscope captured and recorded the emissions. The resultant image resolution was .215 μm/pixel. MetaMorph 7.6.2 software (Danaher, Washington, DC) controlled and synchronized the switching of the excitation filters at the light source and the two cameras' acquisition to sequentially obtain GFP and Alexa Fluor 594 emission images at 6 Hz each for a total frame rate of 12 Hz.

Cell culture

MLO-Y4 osteocyte-like cells (a gift from Dr. Lynda Bonewald of the University of Missouri-Kansas City) were grown in α-modified Eagle's medium supplemented with 5% fetal bovine serum and 5% calf serum. Cells were transiently transfected with either EGFP-actin (Clontech, Mountain View, CA) or GFP-ensconsin MT binding (EMTB) domain (a gift from Dr. Chlöe Bulinski of Columbia University) (22) plasmids to visualize the actin or MT networks. Transfection was performed using Lipofectamine PLUS (Invitrogen, Carlsbad, CA) according to the manufacturer's instructions.

Cytoskeletal inhibitor studies

The cells were divided into four groups according to the cytoskeletal inhibitor used. The Actin group was transfected with EGFP-actin, and the actin network was tracked over time ($n = 7$). The Actin+Colchicine group was transfected with EGFP-actin and incubated with 6 μM colchicine (Sigma-Aldrich, St. Louis, MO) to disrupt the MT network, and the actin network was tracked over time ($n = 7$). The MT group was transfected with GFP-EMTB, and the MT network was tracked over time ($n = 7$). The MT+cytoD group was transfected with GFP-EMTB and incubated with 3μM cytochalasin D (cytoD; Sigma-Aldrich) to disrupt the actin network, and the MT network was tracked over time ($n = 7$).

Flow experiments

A laser cutter (Universal Laser Systems, Scottsdale, AZ) was used to cut glass slides (No. 1 thickness; Fisher Scientific, Waltham, MA) into thin microslides to fit into the flow chamber. Cells were trypsinized 24 h after transfection and plated on the microslides for 20 min. The microslides were then incubated in growth medium with or without inhibitors for an additional
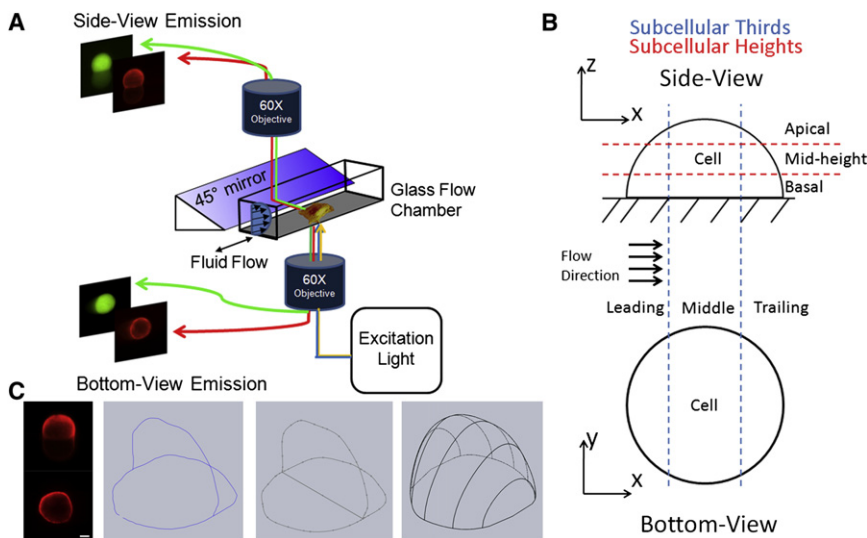

FIGURE 1 (A) Schematic of the quasi-3D microscopy system. (B) Axes for bottom-view and side-view images. Subcellular location divisions are depicted. Subcellular thirds (leading, middle, and trailing) for bottom- and side-views are indicated by blue lines, and subcellular heights (apical, mid-height, and basal) for side-view are shown by red lines. (C) Schematic of conversion of cell plasma membrane boundaries from side and bottom views to obtain a whole-cell volume. Boundary points tracked by digital image correlation are fit to a spline function and then lofted into a 3D shape. Scale bar is 5 μm.

20 min, depending on their assigned cytoskeletal inhibitor group. The microslides were finally incubated in 5μg/mL wheat-germ agglutinin Alexa Fluor 594 (Invitrogen) in Hank's buffered saline solution for 5 min to stain the plasma membrane and then placed in a glass tube to form a flow chamber. The plating time was chosen to ensure fully attached, rounded osteocytes without cellular processes (6,23).

A syringe pump (New Era Pump Systems, Wantagh, NY) and gas-tight syringe (Hamilton, Reno, NV) were used to provide three loading cycles of 10 s of steady fluid flow that generated a shear stress of 10 dynes/cm^2 on the apical surface of the osteocytes with a 10 s rest period between each cycle.

Nonflowed control groups of actin- ($n = 3$) or MT- ($n = 3$) tracked cells were prepared and imaged in the same manner as the flowed groups to measure the baseline amount of cytoskeletal network reorganization and/or movement.

Image analysis

All raw images were first processed in MetaMorph 7.6.2. Bottom- and side-view intensity images of the cytoskeleton and plasma membrane images were first processed with a background intensity subtraction using the average pixel intensity of a region in each image away from the cell, and then further with a 3×3 pixel median filter.

Each cytoskeletal image over time was further processed by means of a digital image correlation technique (24). A normalized cross-correlation algorithm (25) was used to track 16×16 pixel subregions of each image with a center-to-center spacing of 2 pixels against the original image with a zero-order approach using the Image Processing Toolbox in MATLAB 7.8 (The MathWorks, Natick, MA). The subregion size and center-to-center spacing were determined by simulating rigid-body displacement of sample cytoskeletal images and obtaining an accuracy of >99.5% and a standard deviation (SD) < 0.2 pixels of the simulated displacement (26).

The resulting x-y (for bottom-view) and x-z (for side-view) displacement fields (see axis definitions in Fig. 1 B) were each first smoothed using a five-point moving average across the time dimension for each pixel. The displacement fields were then smoothed and differentiated using a 5×5 2D Savitsky-Golay bilinear least-squares filter (27). Finite Lagrangian strain fields were then calculated from the differentiation fields (three bottom-view strains: Eyy, bottom-view Exx, and Exy; and three side-view strains: Ezz, side-view Exx, and Exz) (28). Points within 2 pixels of the edges of the cell were discarded from the analysis due to the square filtering process used. The strain error in the actin images undergoing simulated rigid-body displacement was 0.0192 ± 0.0268 (%). Similarly, the strain error in the MT images was −0.0021 ± 0.0287 (%). The calculated strain error in simulated stretch images was <0.3%.

Each plasma membrane image over time was also processed to obtain the whole-cell volume, as outlined in Fig. 1 C. The initial bottom- and side-view images were thresholded to obtain the points corresponding to the cell membrane boundary. Each point in the outline was tracked over time using the same digital image correlation technique as above. The tracked membrane boundaries in the two views for each time point were oriented in 3D space and then fit to a spline function in Solidworks (Dassault Systèmes, Concord, MA). The cell boundary skeleton was then filled using a lofting algorithm in Solidworks and the volume was obtained, taking advantage of the almost rounded osteocyte shape.

Statistics

All statistical analyses were performed with the use of NCSS 2007 software (NCSS LLC, Kaysville, UT). Because of the large variability between cells, a repeated-measures analysis of variance (ANOVA) was used when appropriate to compare multiple groups. For whole-cell average strain results, the peak strain values at the end of each loading period and residual strain values at the end of each unloading period for all six strain components were collected from each sample. One-tailed t-tests were run to determine

whether the average strain values were tensile or compressive. The significance level, α, was set at 0.05. A repeated-measures ANOVA for each strain parameter with cycle number as a within-subject factor was performed, and a post hoc Tukey-Kramer test was run to determine significance between loading cycles. The Geisser-Greenhouse correction was utilized in the ANOVA when the sphericity assumption was violated. A one-sample t-test of the linear slopes of the peak and residual Exx between side- and bottom-views for each cell was performed to investigate the differences between the two views' Exx values, which were measured simultaneously, but separately, in both views.

To compare subcellular strains, each cell was divided into various subcellular regions, by subcellular thirds in both views (i.e., the leading, middle, or trailing thirds of the cell), or by subcellular height in side-view (i.e., the apical, mid-height, and basal heights; Fig. 1 B). The strains in each location were averaged. An ANOVA with one between-subjects factor (inhibitor) and two within-subjects factors (subcellular region and cycle number) was run between the Actin and Actin+Colchicine groups, and between the MT and MT+cytoD groups. The interactions involving the subject factor were pooled into one error term to achieve more power in the F-tests. Post-hoc Tukey-Kramer multiple-comparison tests were run to determine the significance of factors and interactions.

RESULTS

Whole-cell dilatation

The whole-cell dilatation as measured by the plasma membrane-based cell volume over time was <3% in all four groups (Fig. 2). This suggests that the osteocytes were almost incompressible at the shear loading level that was applied. No statistical difference was seen between the four groups' whole-cell volume change over time.

Cytoskeletal network deformation

Sample images of the actin and MT networks before and after flow are shown in Fig. 3. Sample whole-cell actin network strain traces over time are provided in Fig. 4, B and D. Whole-cell MT network strain traces over time are provided in Fig. 5, B and D. The cells show creep behavior
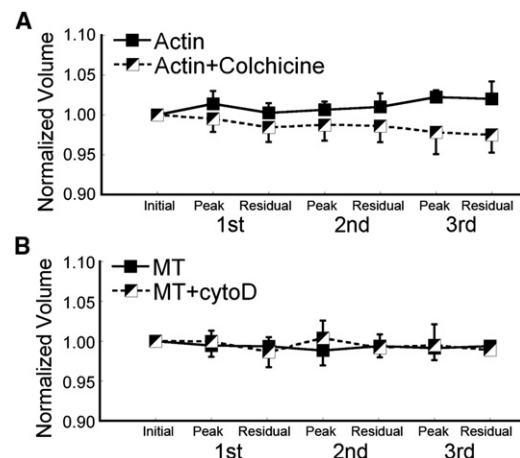

FIGURE 2 Whole-cell volume change over time for (A) actin-tracked groups and (B) MT-tracked groups. No significant differences were observed. Error bars are SDs.
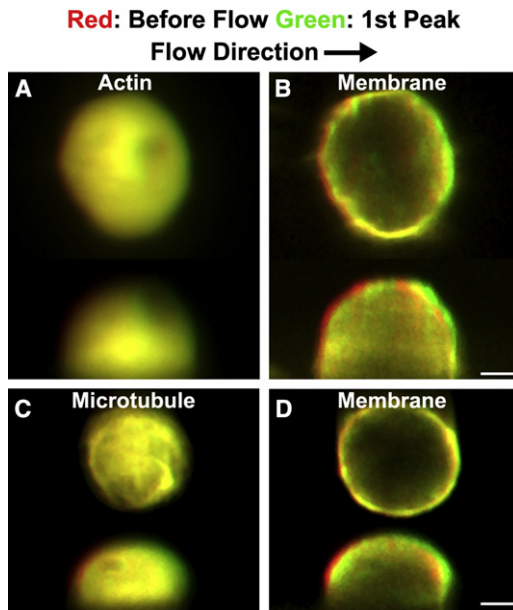
FIGURE 3   Merged fluorescent images of cells before (*red*) and after (*green*) the first loading period in quasi-3D. The osteocyte was transfected to visualize (*A*) actin or (*C*) MT, and counterstained with (*B* and *D*) plasma membrane dye. Flow-induced deformation is apparent in side-view in both dyes. Scale bar is 5 μm.

from the loading and relaxation periods in both networks in both the bottom- and side-views. The strain profiles are clearly time-dependent, emphasizing the necessity of a high temporal resolution to fully capture the instantaneous and short-term behavior of cells under mechanical loading.

Of interest, shear strain was only seen in side-view. The bottom-view shear Exy in most cells hovered near zero, whereas shear Exz in side-view showed significant creep and creep recovery. Side-view strains that measured height (Ezz), flow-directional (side-view Exx), and shear deformations were on the same order of magnitude as the bottom-view strains. These results highlight the 3D deformational behavior of osteocytes under fluid flow in both actin and MT networks.

Actin strain contour plots at the end of the first loading period are provided in Fig. 4, *C* and *E*. MT strain contour plots are provided in Fig. 5, *C* and *E*. The fine-grain heterogeneity of the high compressive or tensile strains varied between individual cells, emphasizing the variability of cellular mechanical properties and cytoskeletal network distribution at the single-cell level. No statistical difference was seen between bottom-view Exx and side-view Exx, although they were separate, independent measurements.

The nonloaded actin and MT network strain magnitudes were $\leq 0.4\%$ after a mock 65 s flow period (data not shown), demonstrating that cytoskeletal rearrangement and movement at the network scale were relatively insignificant over the given time period.

The actin and MT networks were distributed perinuclearly in rounded osteocytes (see Fig. S1 in the Supporting
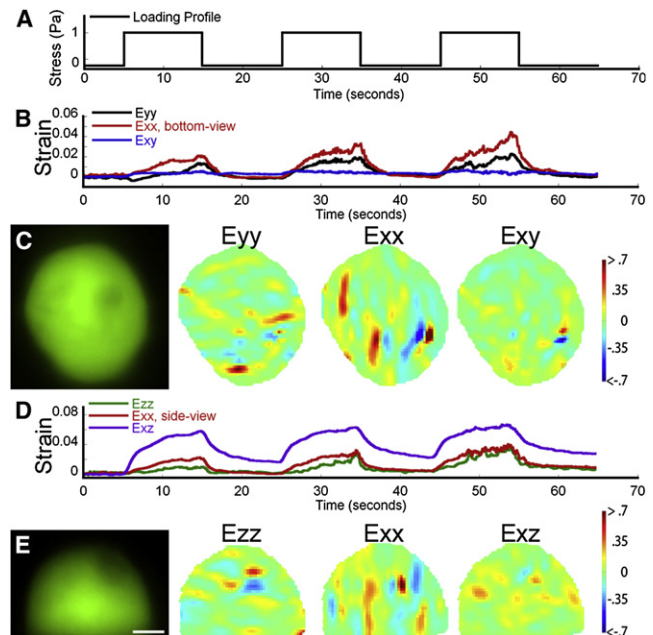

FIGURE 4   Actin network strain traces and contour plots for a sample osteocyte. (*A*) Flow pattern. (*B*) Sample trace of Eyy, Exx, and Exy of the osteocyte obtained in bottom-view. (*C*) Bottom-view image of the osteocyte in *B* and strain contour plots from the first peak. (*D*) Sample trace of Ezz, Exx, and Exz of the osteocyte obtained in side-view. (*E*) Side-view image of the osteocyte and strain contour plots from the first peak. Scale bar is 5 μm.

Material). The actin networks were predominantly cortically distributed and immediately outside the nucleus, whereas the MT networks were more diffusely spread throughout the cell.

Whole-cell actin strains

Whole-cell average strains for the actin-tracked networks treated with or without colchicine to disrupt the MTs are summarized in Fig. 6. Overall, the peak strains in the untreated Actin group were almost always tensile, and the residual strains were always lower than the peak strains. Peak and residual strains tended to increase with cycle for most strains. No trend for Eyy was seen in the Actin group (Fig. 6 *A*). For side-view strains (Fig. 6, *B–D*), the residual strains were tensile, suggesting that the relaxation period was insufficient for the actin network to return to its original state, highlighting the viscoelastic nature of the actin network.

The effect of MT disruption on actin network strains was varied, with some cells having compressive whole-cell peak strains, and there was no consistent trend among the cells in the Actin+Colchicine group. Addition of colchicine caused the Eyy peak strains to be tensile over all loading cycles (Fig. 6 *A*). An effect of colchicine was clearly seen in Ezz (Fig. 6 *C*). Although the peak Ezz and residual Ezz in the Actin group were tensile, strains in the Actin+Colchicine
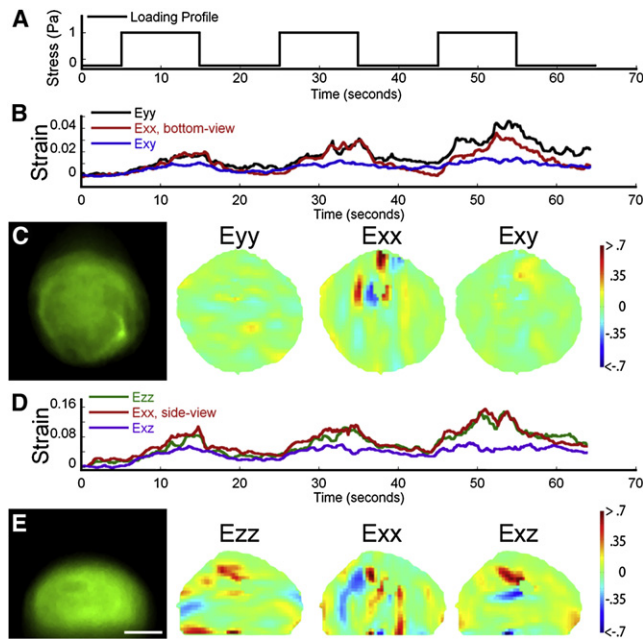
FIGURE 5 MT network strain traces and contour plots for a sample osteocyte. (*A*) Flow pattern. (*B*) Sample trace of Eyy, Exx, and Exy of the osteocyte obtained in bottom-view. (*C*) Bottom-view image of the osteocyte in (*B*) and strain contour plots from the first peak. (*D*) Sample trace of Ezz, Exx, and Exz of the osteocyte obtained in side-view. (*E*) Side-view image of the osteocyte and strain contour plots from the first peak. Scale bar is 5 μm.

group were not different than zero, because some cells in this group had compressive whole-cell Ezz.

Whole-cell MT strains

Whole-cell average strains for the MT-tracked networks treated with or without cytoD to disrupt the actin are summarized in Fig. 7. The untreated MT peak and residual strains were tensile and the residual strains increased with cycle, suggesting that the cells were not able to fully recover in the given relaxation period. This tensile, viscoelastic effect was more apparent than in the actin networks.

Actin disruption by cytoD abolished this effect in the MT+cytoD bottom-view Exx (Fig. 7 *A*). However, the other strains (Fig. 7, *B–D*) remained mostly unaffected by the actin disruption.

Subcellular cytoskeletal strains

The side-view thirds strain distributions and effects of cytoskeletal disruption are summarized in Fig. 8. In the actin networks, regional strain field heterogeneity was seen in Exx and Exz (Fig. 8, *B* and *C*). The effects of MT disruption were greatest in the leading edge to flow in Ezz and side-view Exx strains, and strain field heterogeneity was lost in Exx (Fig. 8, *A* and *B*). MT disruption had no effect on the Exz strain field distribution (Fig. 8 *C*).

In the MT networks, regional strain field heterogeneity was seen only in Exz (Fig. 8 *F*). MT Exx increased in the leading edge but decreased in the trailing edge when actin was disrupted (Fig. 8, *E*). Actin disruption caused MT Exz to increase in the middle of the cell, and strain field distribution heterogeneity was lost (Fig. 8 *F*). No effect was seen in MT Ezz (Fig. 8 *D*).

The strain distributions for different heights of the cell in side-view are summarized in Fig. 9. Actin Exx and Exz were highest in the mid-height of the cell (Fig. 9 *B* and *C*). MT disruption lowered the actin Ezz strain in the mid-height and basal regions of the cell (Fig. 9 *A*) and the actin Exx strain in the mid-height (Fig. 9 *B*). Of interest, Exz was similar in both actin and MT networks (Fig. 9, *C* and *F*), and disruption of either network did not affect the regional strain field heterogeneity.

In summary, the normal Ezz and Exx strains were heterogeneously distributed regionally in the actin networks but not in the MT networks. Shear Exz was similar in both actin and MT networks, showed distinct patterns, and was relatively insensitive to disruption of the counterpart's network.

DISCUSSION

Deformation of the cell and of intracellular cytoskeletal structures under fluid flow has been shown to be spatially heterogeneous and time- and height-dependent (9,16, 29–31). Using the quasi-3D imaging technique, we were able to image osteocytes in two orthogonal planes under fluid flow at a frame rate sufficient to observe the transient, instantaneous mechanical behaviors of the cytoskeletal networks and the whole-cell shape. The high temporal resolution of the system allowed the viscoelastic mechanical behavior to be characterized. To our knowledge, this is the first study to simultaneously investigate the Eyy, Exx, Exy, Ezz, and Exz strain components as measured by cytoskeletal network deformations. The novel side-view observations emphasize the 3D deformational behavior under fluid flow. Shear deformation was visible only in side-view: whereas the bottom-view shear Exy was negligible, the side-view shear Exz was on the same order of magnitude as the flow-directional strains. Furthermore, the quasi-3D technique is not limited to only the osteocyte cell type as studied here; its versatility allows it to be used in other cell-mechanics studies that require spatiotemporal resolution (e.g., to view endothelial cells or the primary cilia under fluid flow).

The plasma membrane dye showed that the cells did not experience a significant amount of dilatation under flow, demonstrating low cellular compressibility under physiological levels of loading. A previous study observed highly compressible whole-cell behavior, but only at very high supraphysiological levels of shear loading (32).

At the whole-cell level (Figs. 6 and 7), the actin and MT networks behaved as viscoelastic materials undergoing primarily tensile creep and creep recovery behaviors
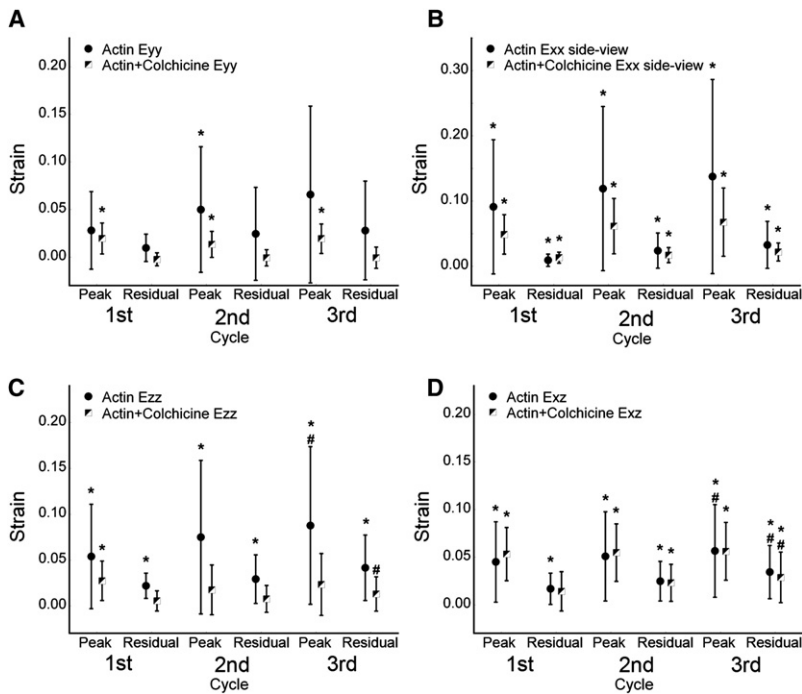
FIGURE 6 Actin and Actin+Colchicine whole-cell average strains for (A) Eyy, (B) Exx side-view, (C) Ezz, and (D) Exz. *Strain is tensile (>0), $p < .05$. [#]The third cycle's peak/residual strain is greater than the first cycle's respective peak/residual strain, $p < .05$. Error bars are SDs.

similarly to most biological materials. Actin and MTs have generally been considered as prestressed tension and compression elements, respectively, when the cell is in an equilibrium, resting state (33). MTs have been shown to act as compression struts to balance the tensile actin prestresses inside a cell (34). In this study, we focused on the dynamic, load-induced deformation of these two networks and showed that the MT network can experience tensile incremental strains under fluid flow in relation to

its equilibrium, baseline prestressed state. Residual strains after the 10 s relaxation periods were more prevalent in the MT networks than in the actin networks, in agreement with previous studies on the timescales of recovery in reconstituted cytoskeletal networks (35,36).

Subcellularly, actin cytoskeletal peak normal strains decreased in the leading edge to flow and closer to the coverslip when the MT network was disrupted (Figs. 8, A and B, and 9, A and B). This suggests that removing the MT
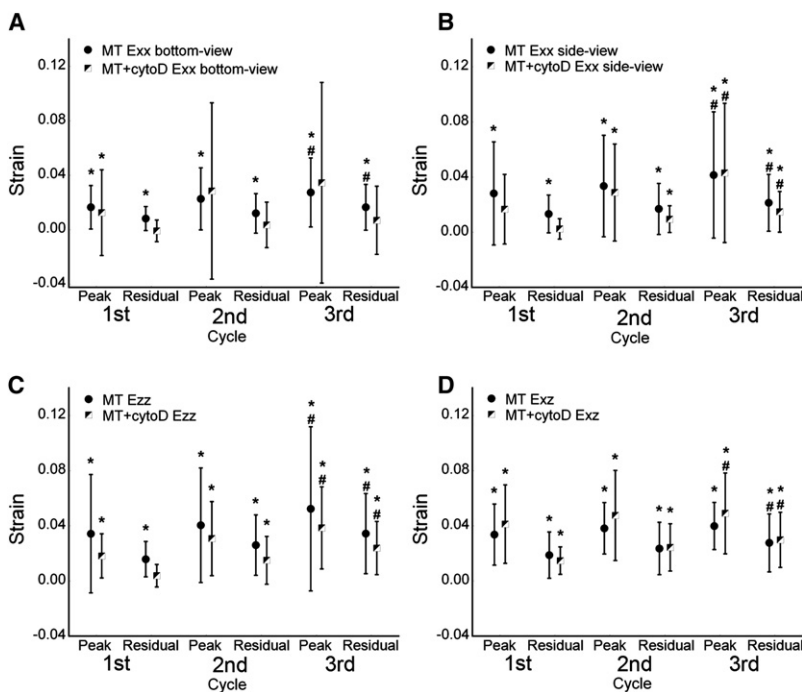

FIGURE 7 MT and MT+cytoD whole-cell average strains for (A) Exx bottom-view, (B) Exx side-view, (C) Ezz, and (D) Exz. *Strain is tensile (>0), $p < .05$. [#]The third cycle's peak/residual strain is greater than the first cycle's respective peak/residual strain, $p < .05$. Error bars are SDs.
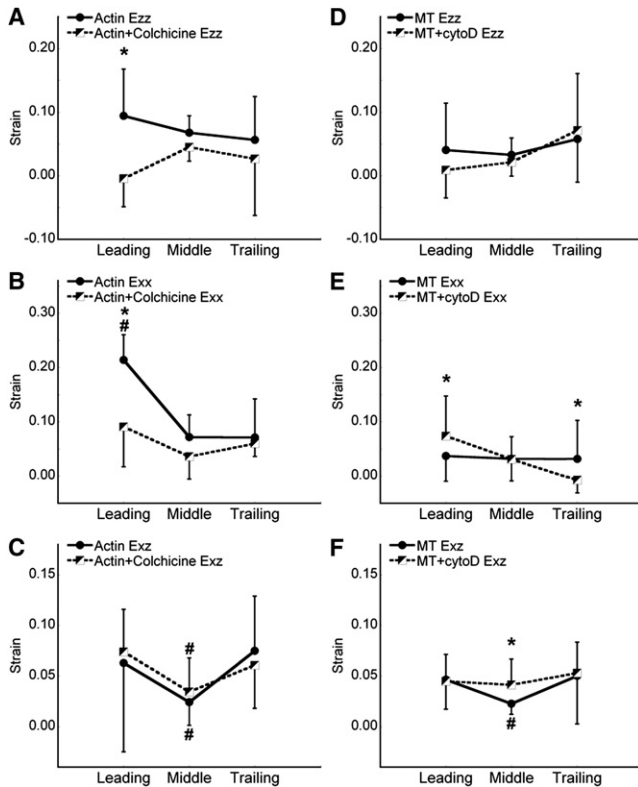
FIGURE 8 Drug and subcellular-third location interactions in the actin network-tracked strains (*A*–*C*) and MT network-tracked strains (*D*–*F*). (*A* and *D*) Ezz strains. (*B* and *E*) Side-view Exx strains. (*C* and *F*) Exz strains. *Statistically significant difference of the strains at a given subcellular third location between groups. #Strain at location is significantly different from other subcellular third locations within that group. Error bars are SDs.

FIGURE 9 Drug and side-view heights location interactions in the actin network-tracked strains (*A*–*C*) and MT network-tracked strains (*D*–*F*). (*A* and *D*) Ezz strains. (*B* and *E*) Side-view Exx strains. (*C* and *F*) Exz strains. *Statistically significant difference of the strains at a given side-view height location between groups. #Strain at location is significantly different from other height locations within that group. Error bars are SDs.

networks increases cell stiffness and is reflected in the apparent stiffness of the actin network, possibly through a prestress mechanism (37–39). However, reports in the literature regarding the role of MT networks in cell stiffness are varied (32,40,41). MT removal has been shown in some cases to increase cell stiffness through this actin prestress balancing mechanism (42). Surprisingly, in our study, actin disruption had little effect on the MT network strain (Figs. 8 and 9).

An interesting finding of this study is that these cytoskeletal changes are location-specific in the osteocyte cytoskeletal networks and are not reflected in the whole-cell strains. Of interest, a previous study on endothelial cells reported no difference in actin network displacement in the leading and trailing edges (43); however, in that study the effects were viewed minutes after the onset of flow. A longer-term study on endothelial cells showed that the stiffness at the leading edge of flow was higher than at the trailing edge after 6 h of flow, and that this was due to actin network rearrangement (30). This emphasizes the time-dependent interactions between the flow field and the cytoskeletal networks. However, the effect of transient, location-
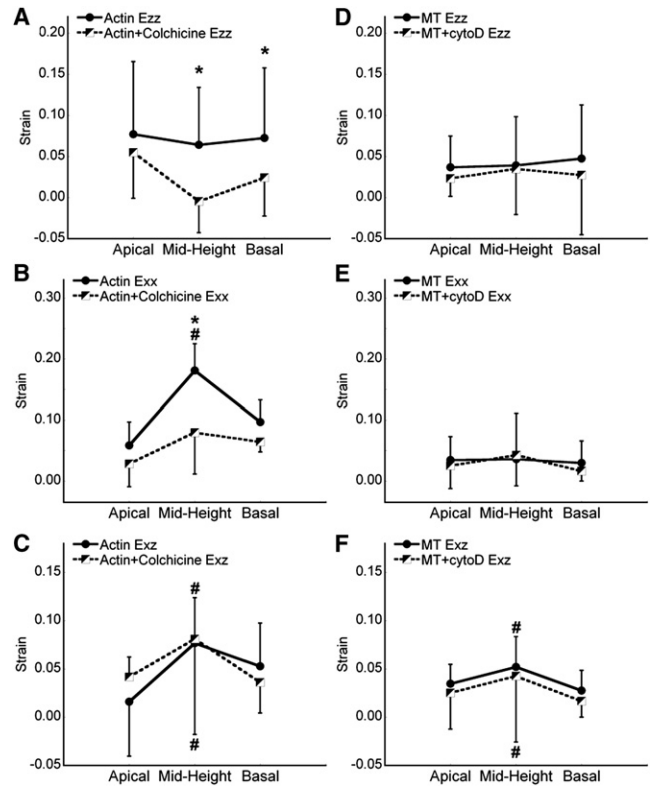
dependent strain patterns on biochemical outputs remains to be determined.

A tradeoff for the high temporal resolution in our study was the loss of optical sectioning of the images. The ~1.3 μm depth of field of the quasi-3D system was confounded by the presence of out-of-focus fluorescent dye from neighboring planes. Consequently, the tracked displacements and resultant strains of the bottom- and side-views came from images that were an average of cellular features in neighboring planes related by the point spread function. The measured strains therefore represent more of an average through many planes rather than of an individual thin slice of the cell.

Tracking the network deformations rather than individual fibers diminished the likelihood of obtaining erroneous strains based on individual filament rearrangement and Brownian motion because the digital image correlation technique tracks the textures of the naturally occurring gradients of the cytoskeletal network. Tracking these textures also lessened the impact of the presence of soluble G-actin, which is not associated with the F-actin networks and can account for up to one-half of the actin in a cell

(44). However, the contribution of small G-actin monomers to the gradients in texture of large cytoskeletal networks is presumably low. This limitation was less important in the MT-tracked groups because the GFP-fusion to the EMTB domain (22) bound to MT filaments and not individual tubulin monomers.

The results obtained with the quasi-3D imaging technique demonstrate the necessity of characterizing the complex spatiotemporal behavior of osteocyte cytoskeletal networks under fluid flow. Future work in correlating the heterogeneous strain deformations to biological outputs, such as mechanosensitive protein kinase activation, will help elucidate the initial events of mechanotransduction from fluid flow. This technique will prove useful for imaging more dynamic, physiological fluid flow profiles, such as oscillatory fluid flow at 1 Hz, in applications where z-stack scanning techniques are unable to accurately image a 3D cell over the flow profile.

SUPPORTING MATERIAL

One figure is available at http://www.biophysj.org/biophysj/supplemental/S0006-3495(10)01060-X.

REFERENCES

1. Taylor, A. F., M. M. Saunders, …, H. J. Donahue. 2007. Mechanically stimulated osteocytes regulate osteoblastic activity via gap junctions. *Am. J. Physiol. Cell Physiol.* 292:C545–C552.

2. You, L., S. Temiyasathit, …, C. R. Jacobs. 2008. Osteocytes as mechanosensors in the inhibition of bone resorption due to mechanical loading. *Bone.* 42:172–179.

3. Tatsumi, S., K. Ishii, …, K. Ikeda. 2007. Targeted ablation of osteocytes induces osteoporosis with defective mechanotransduction. *Cell Metab.* 5:464–475.

4. Jacobs, C. R., C. E. Yellowley, …, H. J. Donahue. 1998. Differential effect of steady versus oscillating flow on bone cells. *J. Biomech.* 31:969–976.

5. Vatsa, A., R. G. Breuls, …, J. Klein-Nulend. 2008. Osteocyte morphology in fibula and calvaria—is there a role for mechanosensing? *Bone.* 43:452–458.

6. Bacabac, R. G., D. Mizuno, …, T. H. Smit. 2008. Round versus flat: bone cell morphology, elasticity, and mechanosensing. *J. Biomech.* 41:1590–1598.

7. Wang, Y., L. M. McNamara, …, S. Weinbaum. 2007. A model for the role of integrins in flow induced mechanotransduction in osteocytes. *Proc. Natl. Acad. Sci. USA.* 104:15941–15946.

8. Adachi, T., Y. Aonuma, …, H. Kamioka. 2009. Calcium response in single osteocytes to locally applied mechanical stimulus: differences in cell process and cell body. *J. Biomech.* 42:1989–1995.

9. Helmke, B. P., A. B. Rosen, and P. F. Davies. 2003. Mapping mechanical strain of an endogenous cytoskeletal network in living endothelial cells. *Biophys. J.* 84:2691–2699.

10. Ajubi, N. E., J. Klein-Nulend, …, E. H. Burger. 1996. Pulsating fluid flow increases prostaglandin production by cultured chicken osteocytes—a cytoskeleton-dependent process. *Biochem. Biophys. Res. Commun.* 225:62–68.

11. Ponik, S. M., J. W. Triplett, and F. M. Pavalko. 2007. Osteoblasts and osteocytes respond differently to oscillatory and unidirectional fluid flow profiles. *J. Cell. Biochem.* 100:794–807.

12. Brangwynne, C. P., F. C. MacKintosh, …, D. A. Weitz. 2006. Microtubules can bear enhanced compressive loads in living cells because of lateral reinforcement. *J. Cell Biol.* 173:733–741.

13. Brangwynne, C. P., G. H. Koenderink, …, D. A. Weitz. 2008. Nonequilibrium microtubule fluctuations in a model cytoskeleton. *Phys. Rev. Lett.* 100:118104.

14. Fletcher, D. A., and R. D. Mullins. 2010. Cell mechanics and the cytoskeleton. *Nature.* 463:485–492.

15. Na, S., O. Collin, …, N. Wang. 2008. Rapid signal transduction in living cells is a unique feature of mechanotransduction. *Proc. Natl. Acad. Sci. USA.* 105:6626–6631.

16. Kwon, R. Y., and C. R. Jacobs. 2007. Time-dependent deformations in bone cells exposed to fluid flow in vitro: investigating the role of cellular deformation in fluid flow-induced signaling. *J. Biomech.* 40:3162–3168.

17. Cao, J., S. Usami, and C. Dong. 1997. Development of a side-view chamber for studying cell-surface adhesion under flow conditions. *Ann. Biomed. Eng.* 25:573–580.

18. Dong, C., J. Cao, …, H. H. Lipowsky. 1999. Mechanics of leukocyte deformation and adhesion to endothelium in shear flow. *Ann. Biomed. Eng.* 27:298–312.

19. Leyton-Mange, J., S. Yang, …, C. Dong. 2006. Design of a side-view particle imaging velocimetry flow system for cell-substrate adhesion studies. *J. Biomech. Eng.* 128:271–278.

20. Chaudhuri, O., S. H. Parekh, …, D. A. Fletcher. 2009. Combined atomic force microscopy and side-view optical imaging for mechanical studies of cells. *Nat. Methods.* 6:383–387.

21. Cao, J., B. Donell, …, C. Dong. 1998. In vitro side-view imaging technique and analysis of human T-leukemic cell adhesion to ICAM-1 in shear flow. *Microvasc. Res.* 55:124–137.

22. Faire, K., C. M. Waterman-Storer, …, J. C. Bulinski. 1999. E-MAP-115 (ensconsin) associates dynamically with microtubules in vivo and is not a physiological modulator of microtubule dynamics. *J. Cell Sci.* 112:4243–4255.

23. Takai, E., R. Landesberg, …, X. E. Guo. 2006. Substrate modulation of osteoblast adhesion strength, focal adhesion kinase activation, and responsiveness to mechanical stimuli. *Mol. Cell. Biomech.* 3:1–12.

24. Sutton, M. A., M. Q. Cheng, …, S. R. Mcneill. 1986. Application of an optimized digital correlation method to planar deformation analysis. *Image Vis. Comput.* 4:143–150.

25. Lewis, J. P. 1995. Fast template matching. *In* Vision Interface. Canadian Image Processing and Pattern Recognition Society, Quebec City, Canada. 120–123.

26. Bae, W. C., C. W. Lewis, …, R. L. Sah. 2006. Indentation testing of human articular cartilage: effects of probe tip geometry and indentation depth on intra-tissue strain. *J. Biomech.* 39:1039–1047.

27. Pan, B., H. M. Xie, …, T. Hua. 2007. Full-field strain measurement using a two-dimensional Savitzky-Golay digital differentiator in digital image correlation. *Opt. Eng.* 46:033601.

28. Wang, C. C., J. M. Deng, …, C. T. Hung. 2002. An automated approach for direct measurement of two-dimensional strain distributions within articular cartilage under unconfined compression. *J. Biomech. Eng.* 124:557–567.

29. Ueki, Y., N. Sakamoto, and M. Sato. 2010. Direct measurement of shear strain in adherent vascular endothelial cells exposed to fluid shear stress. *Biochem. Biophys. Res. Commun.* 394:94–99.

30. Sato, M., K. Suzuki, …, T. Ohashi. 2007. Microelastic mapping of living endothelial cells exposed to shear stress in relation to three-dimensional distribution of actin filaments. *Acta Biomater.* 3:311–319.

31. Knight, M. M., Z. Bomzon, …, D. L. Bader. 2006. Chondrocyte deformation induces mitochondrial distortion and heterogeneous intracellular strain fields. *Biomech. Model. Mechanobiol.* 5:180–191.

32. Ofek, G., D. C. Wiltz, and K. A. Athanasiou. 2009. Contribution of the cytoskeleton to the compressive properties and recovery behavior of single cells. *Biophys. J.* 97:1873–1882.

33. Ingber, D. E. 2003. Tensegrity I. Cell structure and hierarchical systems biology. *J. Cell Sci.* 116:1157–1173.

34. Stamenović, D., S. M. Mijailovich, …, N. Wang. 2002. Cell prestress. II. Contribution of microtubules. *Am. J. Physiol. Cell Physiol.* 282:C617–C624.

35. Lin, Y. C., G. H. Koenderink, …, D. A. Weitz. 2007. Viscoelastic properties of microtubule networks. *Macromolecules.* 40:7714–7720.

36. Humphrey, D., C. Duggan, …, J. Käs. 2002. Active fluidization of polymer networks through molecular motors. *Nature.* 416:413–416.

37. Wang, N., I. M. Tolić-Nørrelykke, …, D. Stamenović. 2002. Cell prestress. I. Stiffness and prestress are closely associated in adherent contractile cells. *Am. J. Physiol. Cell Physiol.* 282:C606–C616.

38. Wang, N., K. Naruse, …, D. E. Ingber. 2001. Mechanical behavior in living cells consistent with the tensegrity model. *Proc. Natl. Acad. Sci. USA.* 98:7765–7770.

39. Park, C. Y., D. Tambe, …, J. J. Fredberg. 2010. Mapping the cytoskeletal prestress. *Am. J. Physiol. Cell Physiol.* 298:C1245–C1252.

40. Trickey, W. R., T. P. Vail, and F. Guilak. 2004. The role of the cytoskeleton in the viscoelastic properties of human articular chondrocytes. *J. Orthop. Res.* 22:131–139.

41. Takai, E., K. D. Costa, …, X. E. Guo. 2005. Osteoblast elastic modulus measured by atomic force microscopy is substrate dependent. *Ann. Biomed. Eng.* 33:963–971.

42. Stamenović, D., Z. Liang, …, N. Wang. 2002. Effect of the cytoskeletal prestress on the mechanical impedance of cultured airway smooth muscle cells. *J. Appl. Physiol.* 92:1443–1450.

43. Mott, R. E., and B. P. Helmke. 2007. Mapping the dynamics of shear stress-induced structural changes in endothelial cells. *Am. J. Physiol. Cell Physiol.* 293:C1616–C1626.

44. Alberts, B. 2008. Molecular Biology of the Cell. Garland Science, New York.